Publ. Astron. Soc. Japan **43**, 195–212 (1991)

X-Ray Implications of a Unified Model of Seyfert Galaxies

Hisamitsu AWAKI and Katsuji KOYAMA

Department of Astrophysics, School of Science, Nagoya University, Furo-cho, Chikusa-ku, Nagoya 464-01

Hajime INOUE

The Institute of Space and Astronautical Science, Yoshinodai, Sagamihara, Kanagawa 229

and

Jules P. HALPERN

Columbia Astrophysics Laboratory, Columbia University, 538 West 120th Street, New York, NY 10027, U.S.A.

(Received 1990 November 9; accepted 1991 January 25)

Abstract

We observed 16 Seyfert galaxies, including 9 Seyfert 2 galaxies, with the Ginga satellite. Thirteen of the Seyfert galaxies in our sample have been detected, and the iron line and K-edge structure for these galaxies investigated. Twelve of the thirteen detected galaxies also have a detected iron line. The equivalent width of a Seyfert 1 galaxy is distributed around a mean value of about 173 eV, with a standard deviation of about 40 eV; that for a Seyfert 2 galaxy is scattered from < 80 eV to 1300 eV. Most of the detected galaxies show an absorption feature at the energy of the iron K-edge. The iron column density determined from the iron K-edge structure ranges from $< 10^{17.5}$ cm^{-2} to 2×10^{19} cm^{-2}. Using a Monte Carlo simulation, we found that isotropic X-ray emission within a uniformly distributed gas cannot explain the observed result. The overall distribution of the iron line and the K-edge intensity for all of the galaxies in our sample could be reproduced by using an accretion torus model with a single parameter: the viewing angle to the active galactic nucleus within an accretion torus.

Key words: Iron line; Seyfert galaxies; X-ray spectra.

1. Introduction

Seyfert galaxies are classified into two groups, Seyfert 1 and 2 galaxies, based on the presence or absence of broad emission lines in their optical spectra, respectively. Antonucci and Miller (1985) discovered a faint polarized broad line in the archetypical Seyfert 2 galaxy: NGC 1068. They concluded that the broad line region in NGC 1068 is completely hidden by thick matter; as a result, we have observed only a fraction of the broad-line region which is scattered by electrons over an extended region surrounding the nucleus, resulting in a polarized broad-line component. This result has revived interest in "unified Seyfert models." These models seek to explain the differences between Seyfert 1 and 2 galaxies in terms of a single parameter, the viewing angle.

Observational support for this model has been accumulated in both the optical and X-ray bands. In spectropolarimetry, Miller and Goodrich (1990) discovered faint polarized broad emission lines in other highly polarized Seyfert 2 galaxies: Mkn 3, Mkn 348, Mkn 463E, and NGC 7674. From hard X-ray observations with the Ginga satellite, Koyama et al. (1989) [also Elvis and Lawrence (1988) with EXOSAT data] found an intense iron line with an equivalent width of 1.3 keV for NGC 1068. This result is expected according to the unified model, as was pointed out by Krolik and Kallman (1987). An obscured X-ray luminous nucleus was found in Mkn 348 (Warwick et al. 1989), NGC 4388 (Hanson et al. 1990), Mkn 3 (Awaki et al. 1990), and NGC 4507 (Awaki et al. 1991b). In particular, Mkn 3 and NGC 4507 have large columns of $(4-6)\times10^{23}$ cm^{-2} along our line of sight, which are considered to be transition cases between less obscured Seyfert 2 galaxies such as Mkn 348, and completely absorbed nuclei, like that of NGC 1068.

Prior to the Ginga satellite the iron line was detected from five Seyfert galaxies: NGC 4151 (Matsuoka et al. 1986), Mkn 509 (Morini et al. 1987), NGC 2992, MCG-5-23-16, and NGC 5506 (Mushotzky 1982). Inoue (1985) and Matsuoka et al. (1986) have found that the flux of the iron line from NGC 4151 cannot be explained in terms of the fluorescence of spherical X-ray emission by uniformly distributed matter, and have suggested the existence of non-uniformly distributed matter or X-ray beaming. Since the number of galaxies in the pre-Ginga sample was limited, any attempt to investigate the unified model using iron-line emission has not been realistic. This problem has now been reduced owing to the Ginga satellite, since data concerning about 30 Seyfert galaxies are now available for this purpose. In this paper we compile observational results regarding the iron line as well as the iron edge structure obtained with the Ginga satellite and try to explain the results in terms of a unified accretion torus model with given geometrical parameters.

2. Observations and Data Reduction

The galaxy sample used here was taken from the performance verification phase (PV), target-of-opportunity (TOO), and announcement of opportunity (AO) observations, which include 7 Seyfert 1 galaxies and 9 Seyfert 2 galaxies. These galaxies were selected on the basis of their cataloged X-ray luminosity. Other than the cataloged luminosity, no apriori selection bias was made. These galaxies are listed in table 1 together with relevant observational details. The X-ray spectra of these galaxies were

Table 1. The observation log.

Target Name	Position $(\alpha, \delta)_{1950}$	Type	Redshift	Observed Date	Exposure (s)	Intensity (cts s^{-1})	BDG position $(\alpha, \delta)_{1950}$
Mkn 348	(11.5, 31.7)	2	0.0151	13 Jun 1987	9984	3.6	(13.2, 28.3)
Mkn 573	(25.4, −2.1)	2	0.0171	24 Dec 1989	6784	< 1	...
NGC 1068	(40.0, −0.2)	2	0.0037	30 Jul 1987	36000	2.8	...
Mkn 3	(92.5, 71.1)	2	0.0137	27 Sep 1989	11648	2.5	...
Mkn 78	(114.5, 65.3)	2	0.0372	20 Oct 1987	15360	< 1	...
NGC 3516	(165.8, 72.8)	1	0.085	7 Oct 1989	8064	10.6	...
NGC 4051	(180.2, 44.8)	1	0.0023	14–16 May 1988	22272	8.8	(175.8, 51.8)
NGC 4151	(182.0, 39.7)	1	0.0033	30 May 1987	5760	20.2	(180.9, 42.6)
NGC 4507	(188.2, −39.6)	2	0.012	6 Jul 1990	7936	3.7	(190.7, −36.2)
NGC 4593	(189.2, −5.1)	1	0.0087	25 Jun 1987	9536	14.9	(190.4, −1.2)
MCG-6-30-15	(203.3, −34.0)	1	0.0078	10 Sep 1987	7296	23.5	(198.7, −38.7)
NGC 5548	(213.9, 25.4)	1.5	0.0166	25 Jun 1988	13568	22.4	(210.6, 30.2)
IRAS 15091−2107	(227.3, −21.1)	1	0.044	13 Mar 1989	14464	6.6	(225.3, −24.2)
Mkn 507	(267.2, 68.7)	2?	0.0559	11 Nov 1987	6528	1.5*	(265.0, 71.6)
IRAS 18325−5962	(278.1, −59.4)	2	0.019	13 May 1989	9984	11.2	(275.5, −64.3)
NGC 7674	(351.4, 8.5)	2	0.029	27 Nov 1989	17792	3.3	(354.4, 12.6)

* contaminated by KZ 163 (Seyfert 1 galaxy).

obtained with the Large Area Counters (LAC) on board the X-ray astronomy satellite Ginga. The LAC comprises eight sets of proportional counters covering the energy range of 1.5–37 keV with a maximum effective area of 4×10^3 cm^2. The field of view is restricted to $1° \times 2°$ by a mechanical collimator. The observational mode for all galaxies was the MPC-1, which provides 48-energy channel data from each counter (Turner et al. 1989). For most of these galaxies, background observations at positions offset by 3–7 degrees were carried out a few days before or after an on-source observation. Those background positions are also listed in table 1.

Since the X-ray intensities of these galaxies are less than 25 counts s^{-1} (see table 1), we used the data from low background orbits, "Remote Orbits" (see Hayashida et al. 1989). The data from regions of low geomagnetic cut-off rigidity (< 9 GeV c^{-1}) and unusual high background events due to a sudden increase in the charged particle flux were excluded. The integration time for each observation ranged between 5000 and 36000 s.

The non X-ray background (NXB) and cosmic diffuse X-ray background (CXB) were subtracted from on-source data in the following manner. NXB was deduced using data accumulated while the LAC field of view was occulted by the dark Earth. If the background data from a nearby sky position were available, a local CXB spectrum for the relevant X-ray source was constructed from this mean CXB spectrum by normalizing the total flux to that of the nearby sky. The normalizing factor was found to be within the range 0.952–1.127. On the other hand, if nearby background data were not available, we used the mean spectrum of the CXB for background subtraction. Further details concerning the background subtraction procedure were described by Awaki et al. (1991a).

We used only data from the top layer, since the S/N ratio of the top layer is better than that of the combined data (top and mid; Turner et al. 1989) in the energy band near to the iron energy.

3. Analysis and Results

Positive X-ray detections were obtained from all of the sample galaxies, except for the following three Seyfert galaxies: Mkn 78, Mkn 507, and Mkn 573. The pulse-height spectra of these galaxies after background subtraction are given in figure 1. The X-ray spectra were fitted by a power-law function plus an emission line, which added a low-energy turn-off and an edge structure. The model is represented by

$$F(E) = (CE^{-\alpha} + \text{iron line}) \exp(-\sigma_{\text{abs}} N_H) \exp(-\sigma_{\text{Fe-abs}} N_{\text{Fe}}). \quad (1)$$

The cross section of photo-electric absorption by cold matter (σ_{abs}) and absorption by the iron K-edge ($\sigma_{\text{Fe-abs}}$) were taken from Brown and Gould (1970) and McMaster et al. (1970), respectively. N_{H} and N_{Fe} are the column density of hydrogen and iron, respectively.

The ionization state determines the energies of the iron line as well as the K-edge after a redshift correction. Since the galactic latitude of each galaxy is greater than 15° and the axial ratios (a/b) for most of these galaxies are less than 2, the hydrogen column density due to our galaxy and the host galaxy should be comparable to the detection limit ($\sim 10^{21}$ cm^{-2}) of the hydrogen column density.

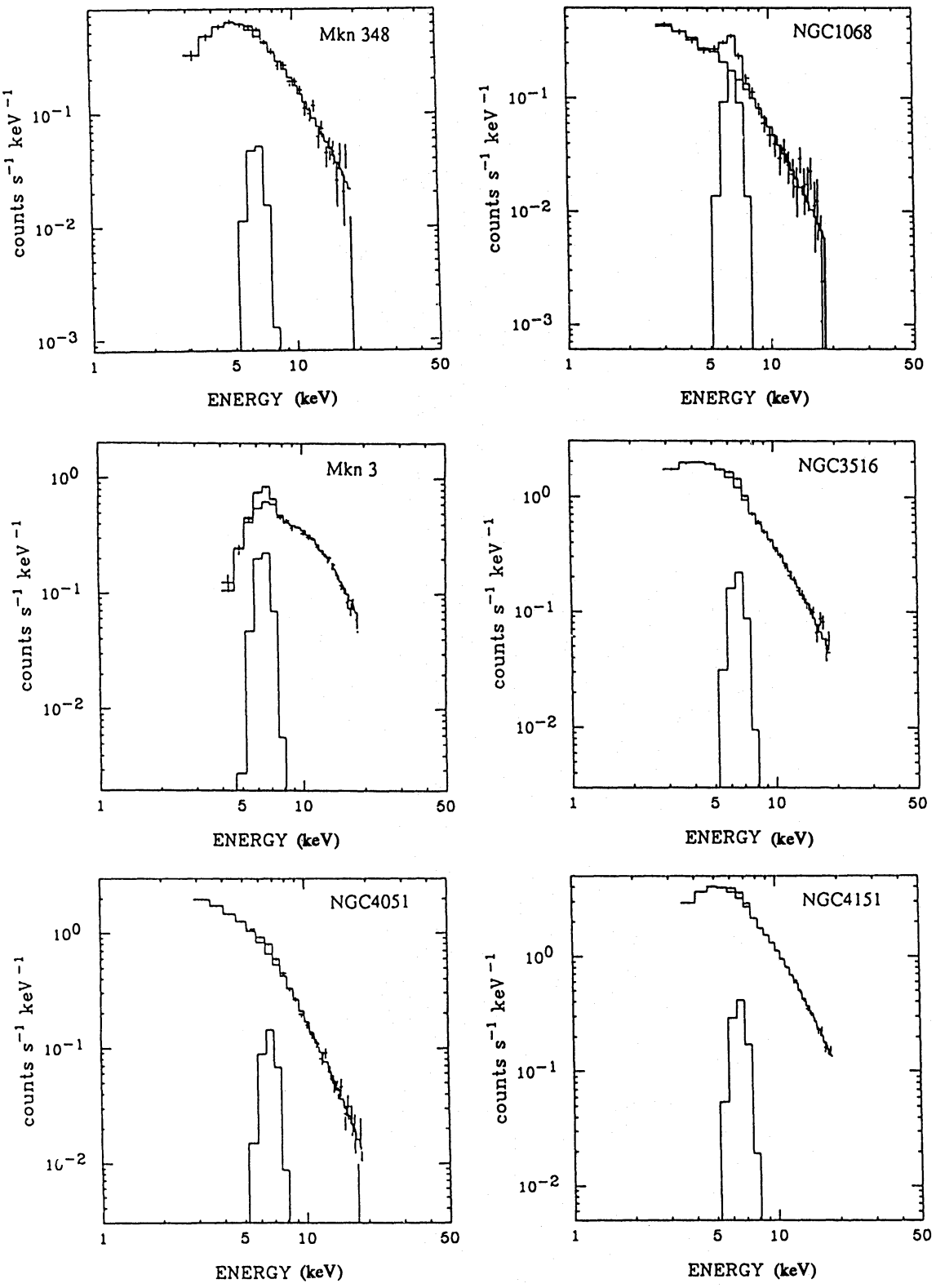

Fig. 1. Pulse-Height spectra of 12 Seyfert galaxies observed with Ginga. The histogram shows the best-fitting spectral model, as described in the text.

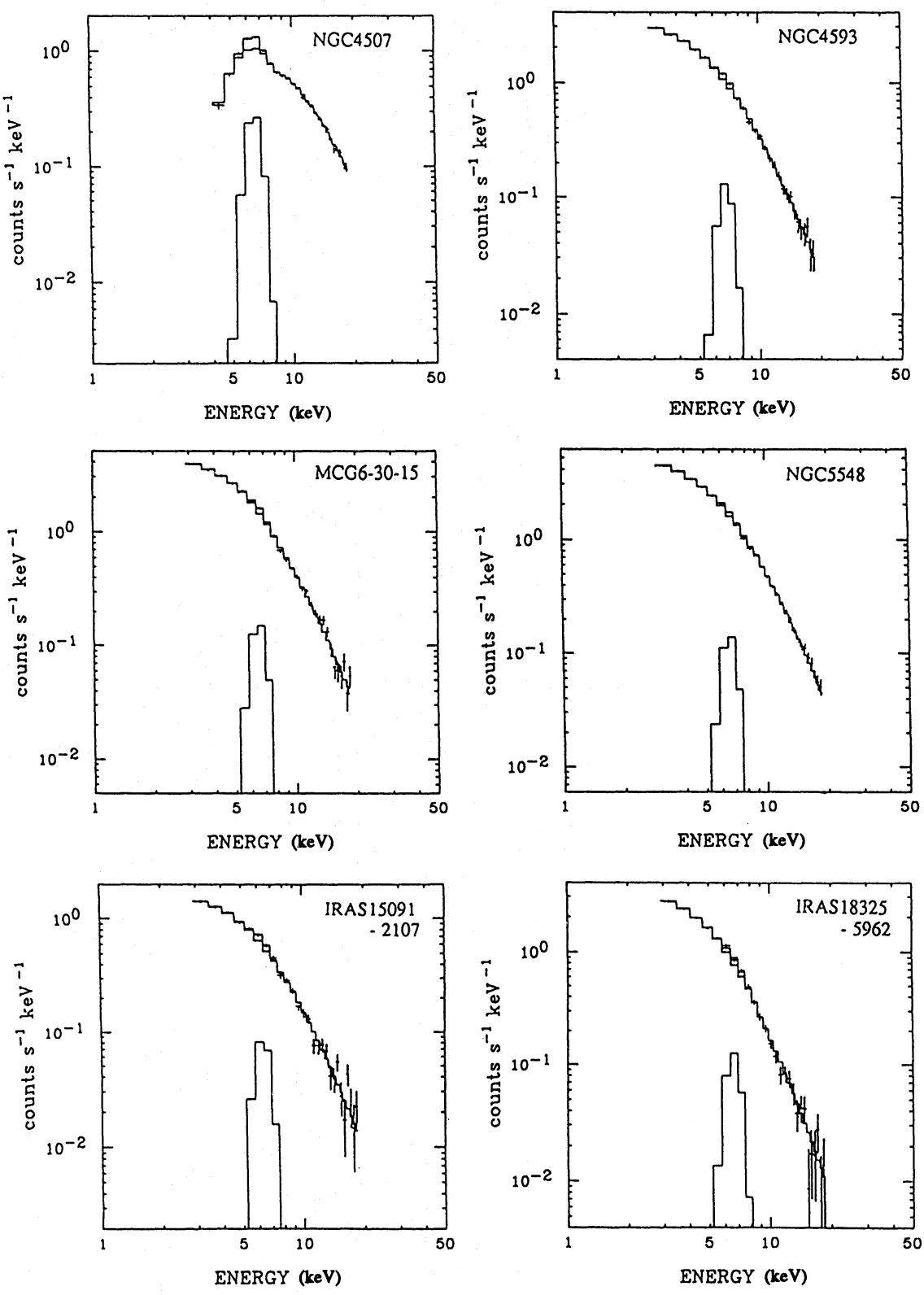

Fig. 1. (Continued)

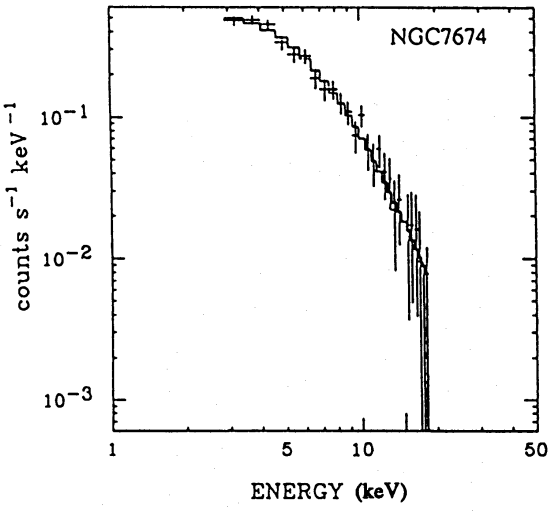

Fig. 1. (Continued)

Since soft excess emission, which can be explained in terms of thermal bremsstrahlung emission with kT ~0.15–0.4 keV, has been reported regarding some Seyfert galaxies (e.g., Turner and Pounds 1989), we have excluded data in the low-energy band for a fit to the single power-law model. Thus, the spectra were fitted within the energy band between about 3 and 19 keV. This fitting was acceptable with the best-fit parameters listed in table 2.

The photon indices obtained from the fitting procedure were distributed around a mean value of $\alpha = 1.62$ with a standard deviation of $\sigma_\alpha = 0.27$. This is consistent with the results of Mushotzky et al. (1980) as well as those of Turner and Pounds (1989). The iron line was detected in all of the Seyfert galaxies in our sample, except for NGC 7674, for which an upper limit of 80 eV was obtained. The equivalent width (EW) of the iron line for Seyfert 1 galaxies was distributed about a mean value of EW=173 with a standard deviation $\sigma_{\rm EW} = 40$, while those for Seyfert 2 galaxies were scattered from < 80 eV to 1300 eV. Figure 2 shows the distribution of EW for the iron line.

The ionization state is a parameter which determines the condition of the iron-emitting region. It is likely that iron is ionized for half of our sample at a 1σ confidence level; except for NGC 4051, NGC 4593, and IRAS 18325−6962, the assumption of neutral iron was not rejected at a 90% confidence level. In order to determine the ionization state, we require a detector with good energy resolution.

Since the energy resolution of the LAC is about 20% at 6 keV and the energy gap between the iron K line and the K-edge is 0.7 keV in neutral iron, the profile of the iron line might couple to the K-edge absorption feature. We therefore estimate the two-parameter error following Lampton et al. (1976). The confidence regions at 1σ level ($\chi^2_{\rm min} + 2.3$) with the interesting two-parameter are shown in the contour map of figure 3, where the contour for NGC 7674 is excluded since the confidence region of the EW and $N_{\rm Fe}$ was very large and, thus, yielding poor statistics.

Table 2. The spectral fit results.

Target Name	L_x (2–10 keV) [a]	Spectral Shape					
	(erg s^{-1})	Photon Index	log (N_H [b])(cm^{-2})	EW (eV)	I. State	log (N_{Fe} [c])(cm^{-2})	χ^2 (d.o.f.)
Mkn 348	2×10^{43}	1.37±0.11	$23.05^{+0.07}_{-0.09}$	150±60	<22	18.6< 18.8	25.6 (21)
NGC1068	4×10^{41}	$1.46^{+0.06}_{-0.05}$	<21.7	1300±100	22±1	<17.6	18.1 (21)
Mkn 3	4×10^{43}	1.49±0.20	23.85±0.03	550±70	13±1	$19.46^{+0.06}_{-0.10}$	22.9 (20)
NGC 3516	1×10^{43}	$1.51^{+0.05}_{-0.04}$	<22.1	220±40	<7	19.11±0.06	18.0 (21)
NGC 4051	5×10^{41}	$1.97^{+0.04}_{-0.03}$	<21.7	230±30	20^{+2}_{-3}	$18.6^{+0.1}_{-0.2}$	23.3 (21)
NGC 4151	5×10^{42}	$1.48^{+0.03}_{-0.04}$	$23.05^{+0.03}_{-0.02}$	160±20	10^{+3}_{-4}	19.00±0.06	12.8 (20)
NGC 4507	4×10^{43}	$1.39^{+0.13}_{-0.19}$	23.70±0.04	400±50	10^{+2}_{-3}	19.3±0.1	22.7 (19)
NGC 4593	1×10^{43}	$1.64^{+0.03}_{-0.02}$	<21.3	170±30	24^{+1}_{-3}	<17.6	17.7 (21)
MCG-6-30-15	2×10^{43}	1.73±0.02	<21.4	130±20	<16	18.5±0.1	32.3 (21)
NGC 5548	6×10^{43}	1.64±0.01	<21.2	110±20	<22	<17.6	26.1 (21)
IRAS 15091−2107	1×10^{44}	$1.75^{+0.06}_{-0.04}$	<22.0	190±40	<22	18.2<18.4	27.7 (21)
IRAS 18325−5962	5×10^{43}	$2.34^{+0.05}_{-0.06}$	<22.1	210±40	22^{+2}_{-3}	$18.8^{+0.1}_{-0.2}$	23.6 (21)
NGC 7674	3×10^{43}	$1.42^{+0.16}_{-0.08}$	<22.2	<80	···	<18.4	19.3 (21)

The errors are 1σ confidence region.
a : $H_0 = 50$ km s^{-1} Mpc^{-1}
b : the hydrogen column density estimated from low cut.
c : the iron column density estimated from the iron edge.

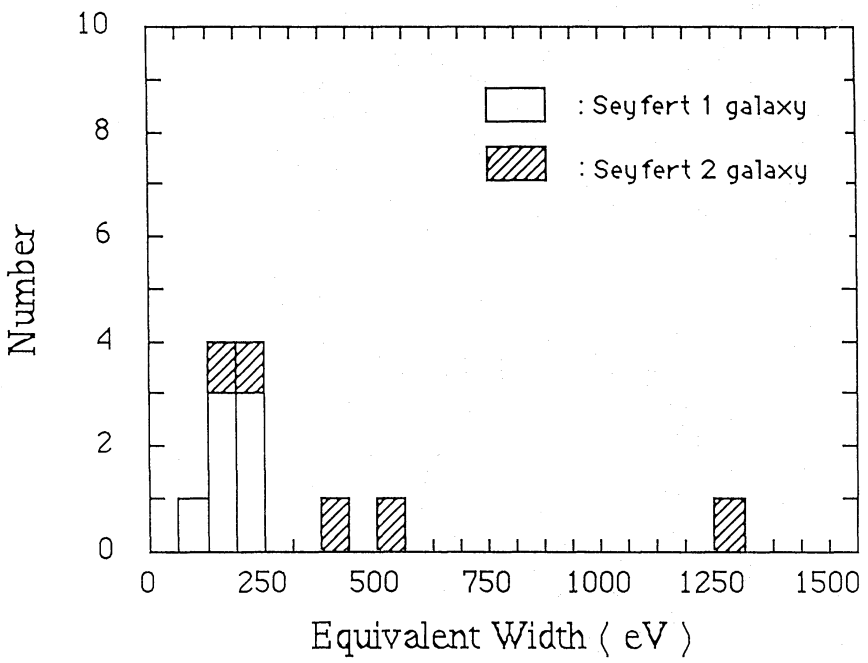

Fig. 2. Distribution of the equivalent width of the iron line. The unhatched and hatched portions represent the equivalent width of the iron line for Seyfert 1 and Seyfert 2 galaxies, respectively.

4. Discussion

We found that all of our detected sample shows a significant iron-line presence, except for NGC 7674, and that most of these galaxies have the iron K-edge structure. Since the X-ray emission was represented by non-thermal power-law emission, the iron Kα from these galaxies is likely to be produced through the fluorescence of continuum X-rays by surrounding material. Within these constraints, we carried out a Monte Carlo simulation in order to estimate both the iron line and K-edge intensities.

For the simulation, we assumed a power-law emission with a photon index of 1.62, the mean value for the present sample. The cross section of photoelectric absorption ($\sigma_{\rm abs}$) by cold matter and absorption ($\sigma_{\rm Fe-abs}$) by neutral iron were taken from those used in the fitting procedure. The Compton scattering coefficient ($\sigma_{\rm scat}$) was taken from the Klein-Nishina formula. The fluorescence yield and cosmic abundance of iron were taken to be 0.34 and 4×10^{-5}, respectively.

4.1. Isotropic Radiation Model

We examined the simplest case, in which X-ray radiation from nuclei is isotropic and the gas distribution is spherically symmetric. The EW of the fluorescence iron line was obtained as a function of $N_{\rm Fe}$. The result is shown in figure 3. EW increases almost linearly with increasing $N_{\rm Fe}$. The EW of this model is about 20 eV at $N_{\rm Fe} \sim 10^{18}$ cm^{-2} which is only about 5% of the observed value. These differences cannot be explained

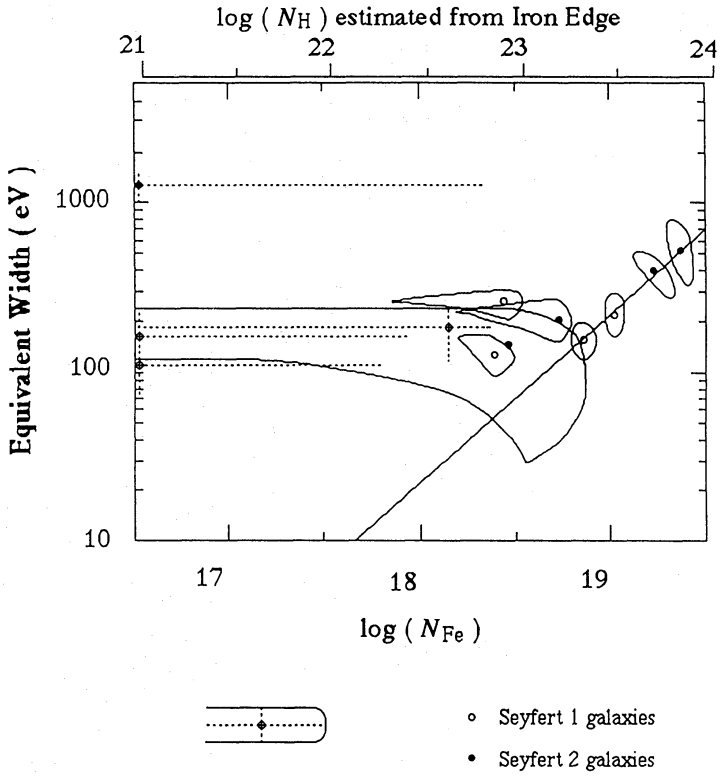

Fig. 3. χ^2 contour map between the equivalent width (EW) of the iron line and the iron column density (N_{Fe}) estimated from the iron edge. The contours are displayed for galaxies which give significant values of the iron line equivalent width and the column density of iron; the contour level is the 1σ confidence level corresponding to $\chi^2_{min} + 2.3$ (Lampton et al. 1976). For the other galaxies, the confidence region is given in the error bar. The open circles and filled circles are for Seyfert 1 and Seyfert 2 galaxies, respectively. The galaxies for which N_{Fe} is an upper limit are shown on the left side (near the column density of $10^{16.6}$ cm^{-2}). The $N_{H\text{-}Fe}$ scale at the top of the figure represents the equivalent hydrogen column density estimated from N_{Fe} by assuming a cosmic abundance of Fe/H=$10^{-4.4}$. The solid line shows the relation between the EW and N_{Fe} in the simplest model: isotropic radiation and uniformly distributed matter.

by an increase in the fluorescence yield of Kα photons with the ionization state. Even the highest yield (from Li-like iron) is only a factor of 2 greater than that for cold material, increasing EW at $N_{Fe} \sim 10^{18}$ to 40 eV, still only 10% of that observed. We thus conclude that this simple model with uniform X-ray emission and gas distribution is unlikely to represent the true situation for the galaxies that we observed.

4.2. Anisotropic Radiation Model

Although in this model we assume that the X-ray emission is either intrinsically anisotropic or beamed, the surrounding gas is still spherically symmetric (see figure 4). If a major component of X-ray flux is detected along our line of sight, the observed X-

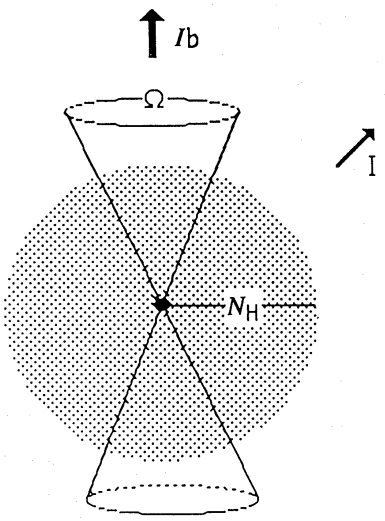

Fig. 4. Schematic view of the anisotropic radiation model. The central filled circle and shaded region represent the X-ray source and the surrounding matter with the hydrogen column density of N_H. The central source radiates an intense X-ray beam (I_b) within a solid angle of Ω. In the other direction it radiates at the level of I.

ray flux is larger than the X-ray flux averaged over 4π sr. Since the iron line intensity should be proportional to the mean flux, the apparent EW becomes smaller than that estimated from an isotropic emission model. This is one possible explanation for the non-detection of the iron line from BL Lac objects (Ohashi et al. 1989). By contrast, if the major X-ray flux is directed away from our line of sight, the apparent EW could be large.

For simplicity we assume that X-ray radiation is beamed within a solid angle, Ω, and that the opacity is much smaller than unity over the energy range from 6 to 50 keV, since the observed hydrogen column density ranges from 10^{22} to 10^{23} cm^{-2}. The EW in this model is approximately given as a function of $\mathrm{EW_{isotropic}}$ (the equivalent width in the case of isotropic radiation):

$$EW \sim \frac{1-\exp(\sigma_{\mathrm{scat}}N_{\mathrm{H}})+\exp(\sigma_{\mathrm{abs}}N_{\mathrm{H}})}{1-\exp(-\sigma_{\mathrm{scat}}N_{\mathrm{H}})+[1/(1+B)]\exp(-\sigma_{\mathrm{abs}}N_{\mathrm{H}})}\mathrm{EW_{isotropic}} \quad (2)$$

$$\sim (1+B)\mathrm{EW_{isotropic}} \qquad \text{if } B \ll \exp(\sigma_{\mathrm{abs}}N_{\mathrm{H}})/[1-\exp(-\sigma_{\mathrm{scat}}N_{\mathrm{H}})].$$

Here, $B = (\Omega/2\pi)\times(I_b/I-1)$, I_b= (the intensity within the radiation cone), I = (the intensity along our line of sight), and σ_{abs} and σ_{scat} are the absorption and scattering cross sections at 6.4 keV, respectively. N_{H} is the hydrogen column density.

Figure 5 shows the relation between parameter B and $\mathrm{EW/EW_{isotropic}}$. For example, in order to obtain an EW of 100 eV at $N_{\mathrm{Fe}} = 10^{17.6}$ cm^{-2}, B should be about 10, assuming cosmic abundance. This corresponds to an I_b/I of about 200 if we take the opening angle of the beam to be 20°. We note that the observed EWs for Seyfert 1 galaxies are within the range 100–200 eV for a wide range of N_{Fe} values. Since $\mathrm{EW_{isotropic}}$ is roughly proportional to N_{Fe}, $(1+B)N_{\mathrm{Fe}}$ for Seyfert 1 galaxies must be

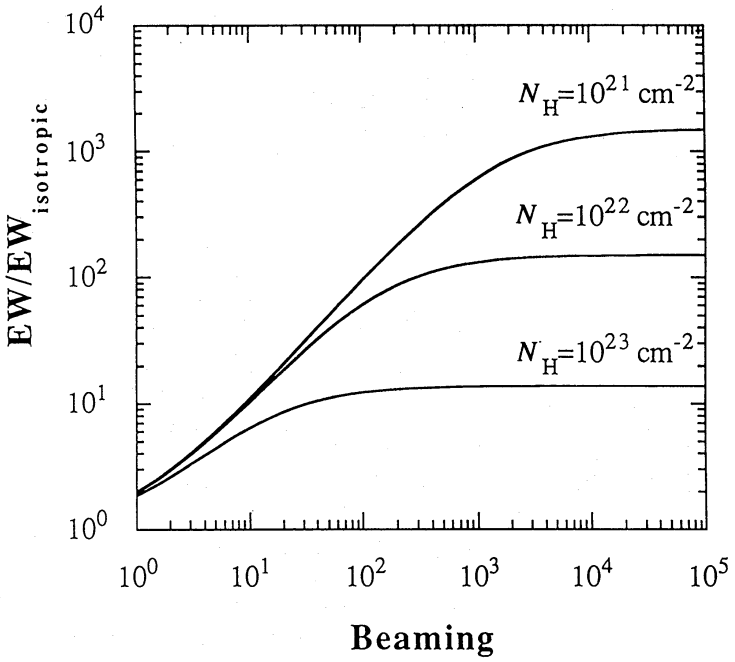

Fig. 5. Discrepancy of the equivalent width (EW) from that in isotropic radiation model due to the beaming effect. The vertical axis shows the ratio between EW in anisotropic radiation and that in isotropic radiation The horizontal axis shows the parameter B which represents the beaming effect (as described in the text).

kept constant at about $10^{18.6}$. We therefore require an artificial fine tuning of B over the wide range of $N_{\rm Fe}$. This reduces the attractiveness of such a model for a general description of Seyfert galaxies.

4.3. Nonuniform Distribution of Surrounding Matter

The intensity of the iron line is proportional to the amount of gas, and the observed column density is strongly dependent on the column density along our line of sight. If the column density along our line of sight is less than that away from our line of sight, the total gas irradiated from central X-ray emission is greater than that estimated from the column density along our line of sight, with an assumption of uniform distribution. It is therefore expected that EW can be large compared to that in uniform distribution at the same column density, and can be kept constant for a wide range of $N_{\rm Fe}$ values when the mean column density away from our line of sight is significantly larger than that along our line of sight.

If the dense matter distributed around a central X-ray emitter avoids our line of sight (implying that the covering factor of the dense matter is nearly unity), the EW of the line is, at most, about 150 eV at a matter density of $N_{\rm Fe} \sim 10^{19}$ cm^{-2} (Inoue 1985). Since the covering factor of every galaxy would be less than unity, the observed EW between 100 and 200 eV cannot be explained. In order to avoid any decrement of the iron line due to self-absorption, Inoue (1989) considered the slab geometry of the surrounding matter, and pointed out that for $N_{\rm Fe} > 10^{19}$ cm^{-2} EW can be $\sim$ 270 eV

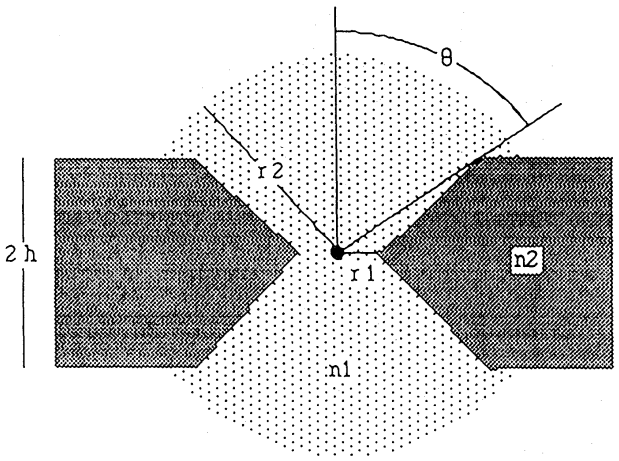

Fig. 6. Cross section of the torus model. The central filled circle represents the X-ray source. The dark shaded region represents an accretion torus with a density on $n2$ (cm^{-3}). The distance between the torus and the central source is $r1$ cm. The height and open angle of the torus are h cm and θ degrees. The gray shaded region within a radius of $r2$ cm is filled by warm gas with a density of $n1$ (cm^{-3}).

at full coverage.

We use a simple model in which the dense matter is distributed away from our line of sight (see figure 6) with a torus geometry. The geometrical parameters given in figure 6 ($\theta, n1, n2, r1, r2$, and h) represent the open angle of the torus, the number density of thin matter along our line of sight, the number density in the torus, the distance of torus from the central source, the radius of thin matter, and the height of the torus, respectively. The product ($n1 \times r2$) corresponds to the column density observed in low-energy photoelectric absorption. The torus geometry can also result in an intense line similar to that in the slab model. Figure 7 shows the EW as a function of $h/r1$. When $h/r1$ is small, the photons emitted from the central source enter the torus perpendicularly, and EW is smallest. This model is consistent with the idealized view of an obscuring torus (thick matter) and an electron scattering region (thin matter) by Krolik and Begelman (1986). For NGC 1068, the temperature in scattering region is $< 10^6$ K according to the polarized-flux line width (Antonucci and Miller 1985).

In a Monte Carlo simulation, the open angle (θ), the iron column density of thin matter ($n1 \times r2$), $h/r1$, and the thickness of torus ($h \times n2$) are taken to be 45°, $10^{17.5}$ cm^{-2}, 10, and 10^{19} cm^{-2}, respectively. The open angle is determined by those of the ionization cones ranging from 30° to 90° (Osterbrock 1990). The column density of thin matter was taken from the value of NGC 1068 (Koyama et al. 1989). The radius (r) of the torus is constrained by the ionization parameter. The ionization parameter (ξ) is expressed as

$$\xi = L/nr^2$$
$$\sim 30(L/10^{43}\ \mathrm{erg\ s^{-1}})(n \times r/10^{23.5}\ \mathrm{cm^{-2}})^{-1}(r/10^{18}\ \mathrm{cm})^{-1}. \quad (3)$$

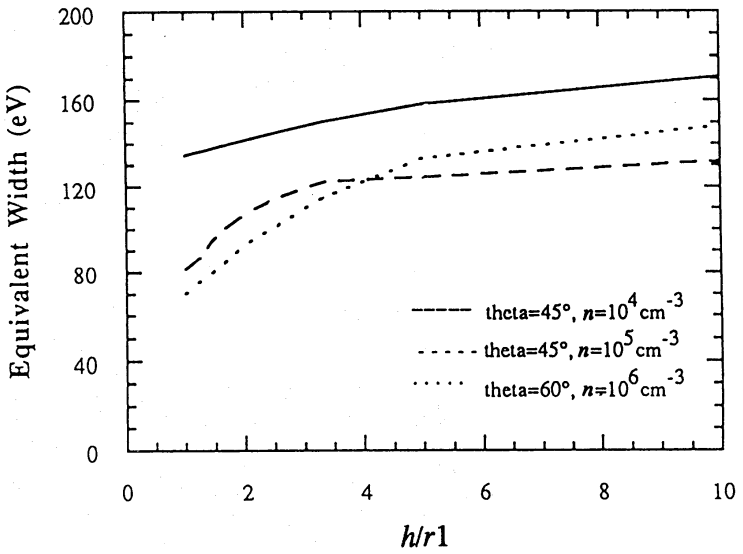

Fig. 7. Equivalent width (EW) of the fluorescent iron line from a torus as a function of $h/r1$. The increasing $h/r1$ corresponds to a smaller photon incident angle. The parameters are described in the text.

For Mkn 3, NGC 4151, and NGC 4507 we found that the iron ionization state is about 10. This state corresponds to $\log \xi = 1.4$ (Kallman and McCray 1982). Assuming $n \times r$ to be $10^{23.5}$H cm^{-2} ($N_{\rm Fe} \times r \sim 10^{19}$ Fe cm^{-2}), the large iron equivalent width for Seyfert 1 galaxy can be explained. The radius of the broad line region has been estimated to be 10^{17} cm at L $\sim 10^{43}$ erg s^{-1} from the photoionization model. The radius of the torus is therefore about 10-times larger than that of the broad-line region, and the accretion torus is placed far from the broad-line region.

By directly looking at the central source from above the torus system, we obtained the spectrum shown by the thick line in figure 8a. This spectrum comprises three components: a direct component, a scattered component, and the iron line. The direct component from the central source is absorbed by thin matter along the line of sight. The scattered component is mainly caused by reflection by the thick torus. Most of the iron line is produced through the fluorescence of continuum X-rays by the thick torus. Fitting this spectrum gave EW, $N_{\rm Fe}$, and $N_{\rm H}$ of 170 eV and $10^{18.2}$ cm^{-2}, and 10^{22} cm^{-2}, respectively. These values are similar to those obtained from the spectra of Seyfert 1 galaxies. The discrepancy between the iron column density ($N_{\rm Fe}$) and the column density along our line of sight ($N_{\rm H}$) is not surprising, since the edge structure is also created by light scattering due to matter outside of our line of sight. A high-energy hump also appears in this spectrum due to the scattered component. This hump agrees with the broad hump predicted by Lightman and White (1988). The presence of this hump was previously noted by Matsuoka et al. (1990) and Pounds et al. (1990) for several Seyfert galaxies through Ginga observations.

When the viewing angle exceeds the open angle of the torus we observe the central source through the edge of the torus: case b) in figure 8. In this case, heavy absorption would be observed. Fitting the spectrum shown in figure 8b, gave EW, $N_{\rm Fe}$, and $N_{\rm H}$ of

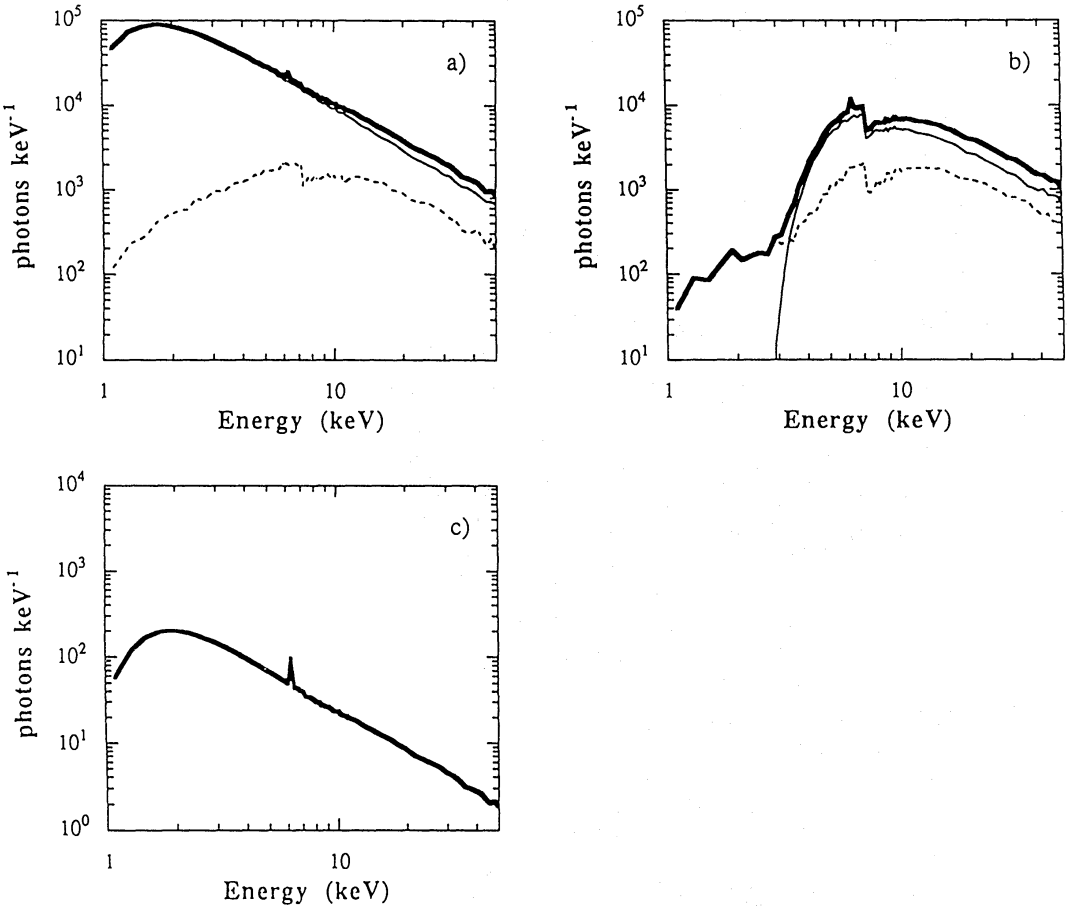

Fig. 8. Spectra obtained from a simulation assuming the torus model. The solid, dashed, and thick-solid lines show the direct component from central source, scattered component, and total observed component, respectively. The difference between these spectra is a result of the viewing angle to central source: a) directly looking at the central source from above the torus system, b) looking through the edge of the torus, and c) looking from the side.

400 eV, $10^{19.5}$ cm^{-2}, $10^{23.8}$ cm^{-2}, respectively. This $N_{\rm Fe}$ of $10^{19.5}$ cm^{-2} is equivalent to an $N_{\rm H}$ of $10^{23.9}$ cm^{-2}, assuming cosmic abundance. This case may correspond to that of NGC 4507 and Mkn 3. In figure 8b we can see the component scattered by upper thin matter in the low-energy band, adding to the reflection component from the thick torus. The scattered components are $\sim$1/1000 of the direct beam, which is consistent with a rough estimation assuming the optical depth of thin matter to be $\tau \sim 0.007$ and the open angle of torus to be $\theta = 45°$.

When this system was observed from the side, the central source was completely hidden by the thick torus. In this case, we observed the scattered component from both the upper and lower thin matter and the fluorescence line produced in the thin matter. Figure 8c shows the expected spectrum in this case. Although the spectral shape was consistent with that of case a), the intensity of the scattered components would be

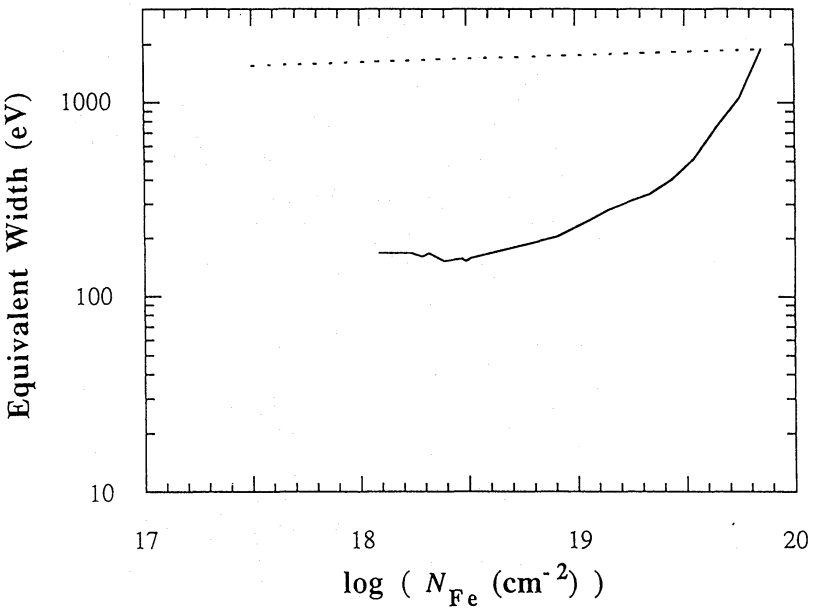

Fig. 9. Equivalent width (EW) of the fluorescent iron line from a torus as a function of N_{Fe} using a Monte Carlo simulation. The geometrical parameters of the torus are described in the text. The solid line shows the change in the two parameters with the viewing angle, showing the transition from case a) to case b) in figure 8. Since the transition between case b) and case c) cannot be simulated, we simply combined the two cases as a dashed line.

$\sim$1/500 of that for case a). The equivalent width of iron line was large (1.1 keV), as was estimated by Krolik and Kallman (1987). This is similar to the observed spectrum for NGC 1068. Non-detected Seyfert 2 galaxies (Mkn 78, Mkn 507, and Mkn 573) with the same flux as those of Mkn 348 and Mkn 3 in the 0.2–4.0 keV band (Kruper et al. 1990) can also be explained as cases in which the observed flux is the scattered component, which is only a small fraction of the intrinsic flux.

We have investigated by simulation the variation of EW and N_{Fe} due to changes in the viewing angle. Figure 9 shows EW as the function of N_{Fe}: EW remains constant at about 170 eV for N_{Fe} in the range 10^{18} to 10^{19} cm^{-2}; it increases as the value of N_{Fe} increases from $10^{19} - 10^{20}$ cm^{-2}. EW follows the observed results up to 10^{20} cm^{-2}. If the hydrogen column density along our line of sight is sufficiently thick to block the direct component, EW must be large (1–2 keV), and N_{Fe} becomes roughly equal to the column density of thin matter. Even though transition between those values cannot be exactly given from the simulation because of poor statistics, the expected N_{Fe} and EW are roughly shown by the dashed line in figure 9. The torus model can explain both the observed EW and N_{Fe} for both Seyfert 1 and Seyfert 2 galaxies. In the torus model, the increase in the column density can be explained as a decrease in the viewing angle of this system.

5. Conclusion

Although the torus model gives a good fit for the overall relation between EW and $N_{\rm Fe}$ from Seyfert 1 to Seyfert 2 galaxies, our result provides no constraint on the distance between the central X-ray source and the accretion torus. The iron line from Seyfert 1 galaxies has been considered to be the fluorescence line from accretion disks (Pounds et al. 1990; George et al. 1990; Inoue et al. 1989); still the accretion torus can be used to naturally explain the intensity of the fluorescence line. This problem will be solved by a systematic study of the variability of the iron line as well as continuum emission.

We thank all of the members of the Ginga team, and especially Dr. H. Kunieda for valuable comments. Thanks are also due to Dr. M. Ward and Dr. C. Done for their critical reading of this manuscript and their comments. The data analysis was performed on the FACOM M380 computer of the high-energy physics laboratory of Nagoya University. This work was partly supported by the Scientific Research Fund of the Ministry of Education, Science, and Culture under Grant No. 02952008 (H.A.).

References

Antonucci, R. R. J., and Miller, J. S. 1985, *Astrophys. J.*, **297**, 621.
Awaki, H., Koyama, K., Kunieda, H., Takano, S., Tawara, Y., and Ohashi, T. 1991a, *Astrophys. J.*, **366**, 88.
Awaki, H., Koyama, K., Kunieda, H., and Tawara, Y. 1990, *Nature*, **346**, 544.
Awaki, H., Kunieda, H., Tawara, Y., and Koyama, K. 1991b, *Publ. Astron. Soc. Japan*, **43**, No. 4, in press.
Brown, J. L., and Gould, R. J. 1970, *Phys. Rev. D*, **1**, 2252.
Elvis, M., and Lawrence, A. 1988, *Astrophys. J.*, **331**, 161.
George, I. M., Nandra, K., and Fabian, A. C. 1990, *Monthly Notices Roy. Astron. Soc.*, **242**, 28P.
Hanson, C. G., Skinner, G. K., Eyles, C. G., and Willmore, A. P. 1990, *Monthly Notices Roy. Astron. Soc.*, **242**, 262.
Hayashida, K., Inoue, H., Koyama, K., Awaki, H., Takano, S., Tawara, Y., Williams, O. R., Denby, M., Stewart, G. C., Turner, M. J. L., Makishima, K., and Ohashi, T. 1989, *Publ. Astron. Soc. Japan*, **41**, 373.
Inoue, H. 1985, in *Japan-US Seminar on Galactic and Extragalactic Compact X-ray Sources*, ed. Y. Tanaka and W. H. G. Lewin (Tokyo:ISAS), p. 283.
Inoue, H. 1989, in *X-Ray Astronomy, Proc. 23rd ESLAB Symp.*, **2**, 783.
Kallman, T. R., and McCray, R. 1982, *Astrophys. J. Suppl.*, **50**, 263.
Koyama, K., Inoue, H., Tanaka, Y., Awaki, H., Takano, S., Ohashi, T., and Matsuoka, M. 1989, *Publ. Astron. Soc. Japan*, **41**, 731.
Krolik, J. H., and Begelman, M. C. 1986, *Astrophys. J. Letters*, **308**, L55.
Krolik, J. H., and Kallman, T. R. 1987, *Astrophys. J. Letters*, **320**, L5.
Kruper, J. S., Urry, C. M., and Canizares, C. R. 1990, *Astrophys. J. Suppl.*, **74**, 347.
Lampton, M., Margon, B., and Bowyer, S. 1976, *Astrophys. J.*, **208**, 177.
Lightman, A. P., and White, T. R. 1988, *Astrophys. J.*, **335**, 57.
Matsuoka, M., Ikegami, T., Inoue, H., and Koyama, K. 1986, *Publ. Astron. Soc. Japan*, **38**, 285.

Matsuoka, M., Piro, L., Yamauchi, M., and Murakami, T. 1990, *Astrophys. J.*, **361**, 440.
McMaster, W. H., Grande, N. K. D., Mallet, J. H., and Hubbell, J. H. 1970, *Compilation of X-ray Cross Sections*, UCRL-50174.
Miller, J. S., and Goodrich, R. W. 1990, *Astrophys. J.*, **355**, 456.
Morini, M., Lipani, N. A., and Molteni, D. 1987, *Astrophys. J.*, **317**, l45.
Mushotzky, R. F. 1982, *Astrophys. J.*, **256**, 92.
Mushotzky, R. F., Marshall, F. E., Boldt, E. A., Holt, S. S., and Serlemitsos, P. J. 1980, *Astrophys. J.*, **235**, 377.
Ohashi, T., Makishima, K., Inoue, H., Koyama, K., Makino, F., Turner, M. J. L., and Warwick, R. S. 1989, *Publ. Astron. Soc. Japan*, **41**, 709.
Osterbrock, D. E. 1990, submitted to *Reports on Progress in Physics.*
Pounds, K. A., Nandra, K., Stewart, G. C., George, I. M., and Fabian, A. C. 1990, *Nature*, **344**, l32.
Turner, M. J. L., Thomas, H. D., Patchett, B. E., Reading, D. H., Makishima, K., Ohashi, T., Dotani, T., Hayashida, K., Inoue, H., Kondo, H., Koyama, K., Mitsuda, K., Ogawara, Y., Takano, S., Awaki, H., Tawara, Y., and Nakamura, N. 1989, *Publ. Astron. Soc. Japan*, **41**, 345.
Turner, T. J., and Pounds, K. A. 1989, *Monthly Notices Roy. Astron. Soc.*, **240**, 833.
Warwick, R. S., Koyama, K., Inoue, H., Takano, S., Awaki, H., and Hoshi, R. 1989, *Publ. Astron. Soc. Japan*, **41**, 739.